Hierarchical Control of Series-Connected String Converter-Based Islanded Electrical Power System

Jinwei He, *Member, IEEE*, Xiaohui Liu, Chaoxu Mu, *Senior Member, IEEE*, and Chengshan Wang, *Senior Member, IEEE*

***Abstract*—Cascaded-connected string converter is an effective way to directly interconnect distributed low-voltage dc sources into higher voltage ac grids. When this system is switched to islanding operation, an important task is to obtain decentralized power sharing among power cells according to the corresponding dc source power capacity, and at the same time, maintaining a good regulation of supply voltage quality to local critical loads. In this paper, a hierarchical control approach is proposed to simultaneously realize the abovementioned two tasks. First, the central controller at point of common coupling (PCC) is responsible for supply voltage magnitude and frequency deviation suppression and it also distributes the key control signals to all power cell local controllers with only low bandwidth communications. At the same time, a modified inverse power factor droop regulator with adjustable offset is adopted by each power cell. As the offset is relevant to the PCC load power factor and the state of charges of power cell backstage batteries, it can easily obtain decentralized proportional power sharing. The proposed system and the control strategy are compared with the conventional parallel converters-based system and the potential applications of the system are also given in this paper.**

***Index Terms*—Frequency compensation, hierarchical control, inverse droop control, microgrids, power sharing, voltage magnitude compensation.**

I. Introduction

THE GROWING installation of distributed renewable energy power sources and energy storage units has stimulated microgrid applications with islanding operation capability. In most of the previous research, an islanded microgrid consists of a few parallel-connected distributed generation (DG) units that operate in a coordinated manner [1]–[4]. As distributed dc source voltage is usually lower than the suitable ranges for direct grid integration using a conventional single-stage dc/ac inverter, two-stage power conversion including a dc/dc boosting and a dc/ac inverting is widely adopted for DG units. In addition, the droop control can be applied to parallel islanded DG units to realize power sharing without any communications among them [5]–[7]. However, it is necessary to note that droop control often suffers from instable problems and the reactive power sharing may have nontrivial errors [8]–[10], due a fact that the feeder impedance is usually unknown and it can be mainly resistive. From the energy conversion perspective, the real power sharing aims to obtain proper energy management among distributed dc sources, such as battery bank, photovoltaic (PV) arrays, and fuel cells. At the same time, the reactive power sharing is not directly involved in the energy management, but a proper reactive power sharing can reduce the supply voltage fluctuations and it can also reduce the circulating current between parallel DG units.

On the other hand, the series-connected string converters have been proposed to directly integrate multiple low voltage dc sources into higher voltage grid in recent studies [11]–[13]. Due to the adoption of single-stage bidirectional dc/ac power conversion in each power cell and the use of low-voltage power switches, the cascaded string converter has been considered as an attractive alternative way for renewable energy and energy storage system grid integration [14]. For instance, the cascaded H-bridge (CHB) converter is used to interconnect multiple PV arrays into power grid and each array has an independent maximum power point tracking control to enhance the solar energy harvesting performance [15], [16]. As the output power of solar array is not fully controllable due to a few factors including radiations and temperature uncertainty, the PV battery hybrid CHB system for better power management was recently proposed in [17]. In addition, the control of three-phase CHB converter with the interphase power flow control via proper zero-sequence voltage injection is proposed for high-power PV integration applications [18].

Note that the previous research mainly focuses on the grid-tied operation of string converters where the output real and reactive power of the string converter can be actively tuned according to the system operation requirement. In addition, a central controller is adopted for independent power control of each power cell with synchronized pulsewidth modulation (PWM) [19]. However, for an islanded microgrid system with a larger number of low-voltage dc power sources that may be far away from each other [20], using such centralized controller is difficult and cost expensive. In addition, considering the power flow principles of parallel DG units and series-connected power cells are very different, it is apparent that the conventional droop control

Manuscript received November 2, 2018; revised February 26, 2019; accepted April 16, 2019. Date of publication April 24, 2019; date of current version October 18, 2019. This work was supported by the National Key R&D Program of China under Grant 2017YFB0902001. Recommended for publication by Associate Editor K. Sun. *(Corresponding author: Chaoxu Mu.)*

The authors are with the School of Electrical Automation and Information Engineering, Tianjin University, Tianjin 300072, China (e-mail: jinwei.he@tju.edu.cn; weliu11@126.com; cxmu@tju.edu.cn; cswang@tju.edu.cn).

Color versions of one or more of the figures in this paper are available online at http://ieeexplore.ieee.org.

Digital Object Identifier 10.1109/TPEL.2019.2913212

cannot be used in this case. In order to overcome these limitations, a fully decentralized inverse droop was recently developed for real power sharing of string converters in islanding operation mode [21]–[23], via using each power cell's power factor as the input of the inverse droop controller. It is important to note that the abovementioned decentralized control methods still have the following limitations: 1) the inverse power factor control may cause nontrivial steady-state point of common coupling (PCC) voltage magnitude and frequency deviations, particularly when a lot of distributed feeders are used to interconnect power cells and the sum of the feeder impedance is high; and 2) only equal power sharing performance is obtained. However, this requirement is relatively rare for practice, due to a fact of varying backstage available power capacity for each power cell.

Motivated by the limitations as mentioned above, an improved hierarchical control approach is proposed to further enhance the performance of string converters-based islanded microgrid. First, the PCC voltage magnitude is compensated by a simple restoration regulator at PCC central controller. At the same time, the weighted average state of charge (SoC) and PCC load power factor are obtained by the central controller and they are sent to all power cells local controllers as calibration coefficients. Second, proportional power sharing between power cells according to their backstage available power ratings is achieved mainly through local control, via a modified inverse power factor droop with adjustable calibration coefficients. Note that each power cell steady-state frequency deviation is compensated by this calibration term in the local controller. Accordingly, the PCC voltage frequency is also passively compensated.

II. Proposed System

Fig. 1 shows the configuration of the proposed series-connected power cells-based islanded microgrid. Each power cell is composed of an H-bridge converter and an output *LC* filter, in order to provide both bidirectional power flow and proper switching ripple mitigation [24], [25]. Then, these string converters are connected in series by feeders. Note that with sufficient number of series-connected power cells, there is no need to have any bidirectional dc/dc boost converter in the power cell and the battery bank can be directly connected to the dc rail of the H-bridge converter. There are also a few loads at PCC.

To obtain a flexible power sharing according to battery SoCs and an accurate PCC voltage magnitude and frequency regulation at the same time, a hierarchical control approach is applied to this system. A detailed introduction to the proposed hierarchical control architecture is given in the following of this section.

A. Central Control

First, a central controller is placed at PCC to monitor the PCC voltage status. Due to the voltage drops on the distributed feeders and the control of power cells with voltage phase angles difference, the PCC voltage may have significant magnitude and frequency deviations. In order to ensure an enhanced supply voltage to loads, a simple restoration controller is adopted by the central controller as

$$g_c = 1 + (E^* - E_{\mathrm{PCC}}) \cdot \left(k_{p\_\mathrm{mag}} + \frac{k_{i\_\mathrm{mag}}}{} \right) \qquad (1)$$

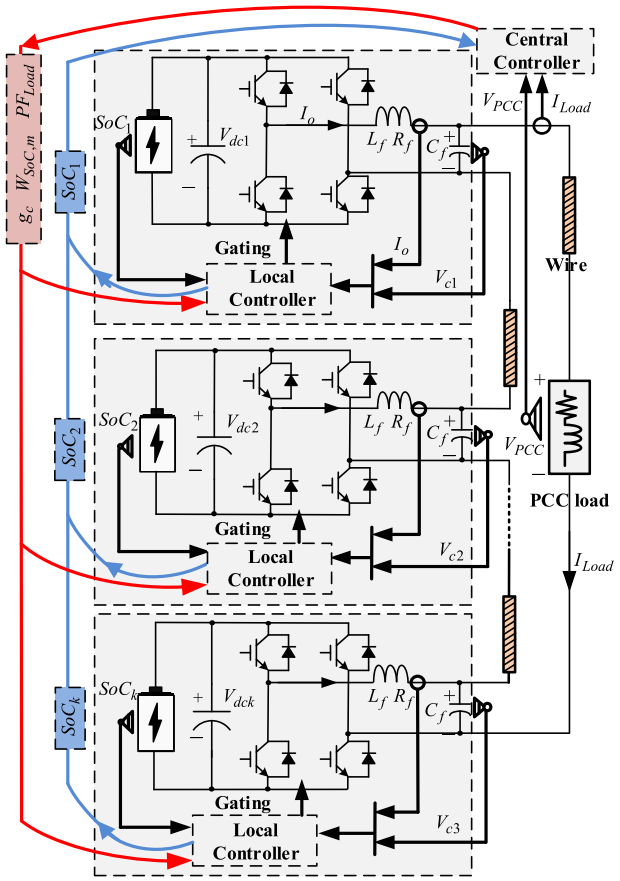

Fig. 1. Diagram of a series-connected H-bridge power cells-based islanded microgrid.

where $\boldsymbol{E^*}$ and $\boldsymbol{E_{PCC}}$ are magnitudes of the reference voltage and the measured PCC voltage, respectively. $\boldsymbol{k_{p\_mag}}$ and $\boldsymbol{k_{i\_mag}}$ are the proportional and integral gains of the PI regulator for PCC voltage magnitude deviation compensation. The output of the controller is a gain $\boldsymbol{g_c}$, which is used to tune each power cell voltage magnitude reference via a low bandwidth (LBC) communication system between the central and the local controllers.

In addition, the central controller at PCC is responsible for collecting status information of all power cells. For the power sharing application as discussed in this paper, the SoC of each power cell is sent to the central controller via the LBC. For practical applications, the backstage batteries are usually designed at the same rated ampere–hour (AH). In this case, the weighted average SoC of each power cell is simply defined as

$$W_{\mathrm{SoC},m} = k \cdot \mathrm{SoC}_m / \sum\nolimits_{n=k} \mathrm{SoC}_n \qquad (2)$$

where $\boldsymbol{SoC_m}$ is the SoC of the power cell m. $\boldsymbol{k}$ is the total number of series-connected power cells. Note that for the applications with different battery AHs, the parameter can also be defined in a similar way.

Furthermore, the central controller also measures the power factor of all PCC loads as $\boldsymbol{PF_{Load}}$. Afterward, the load $\boldsymbol{PF_{Load}}$ and the weighted average $\boldsymbol{W_{SoC,m}}$ of each power cell

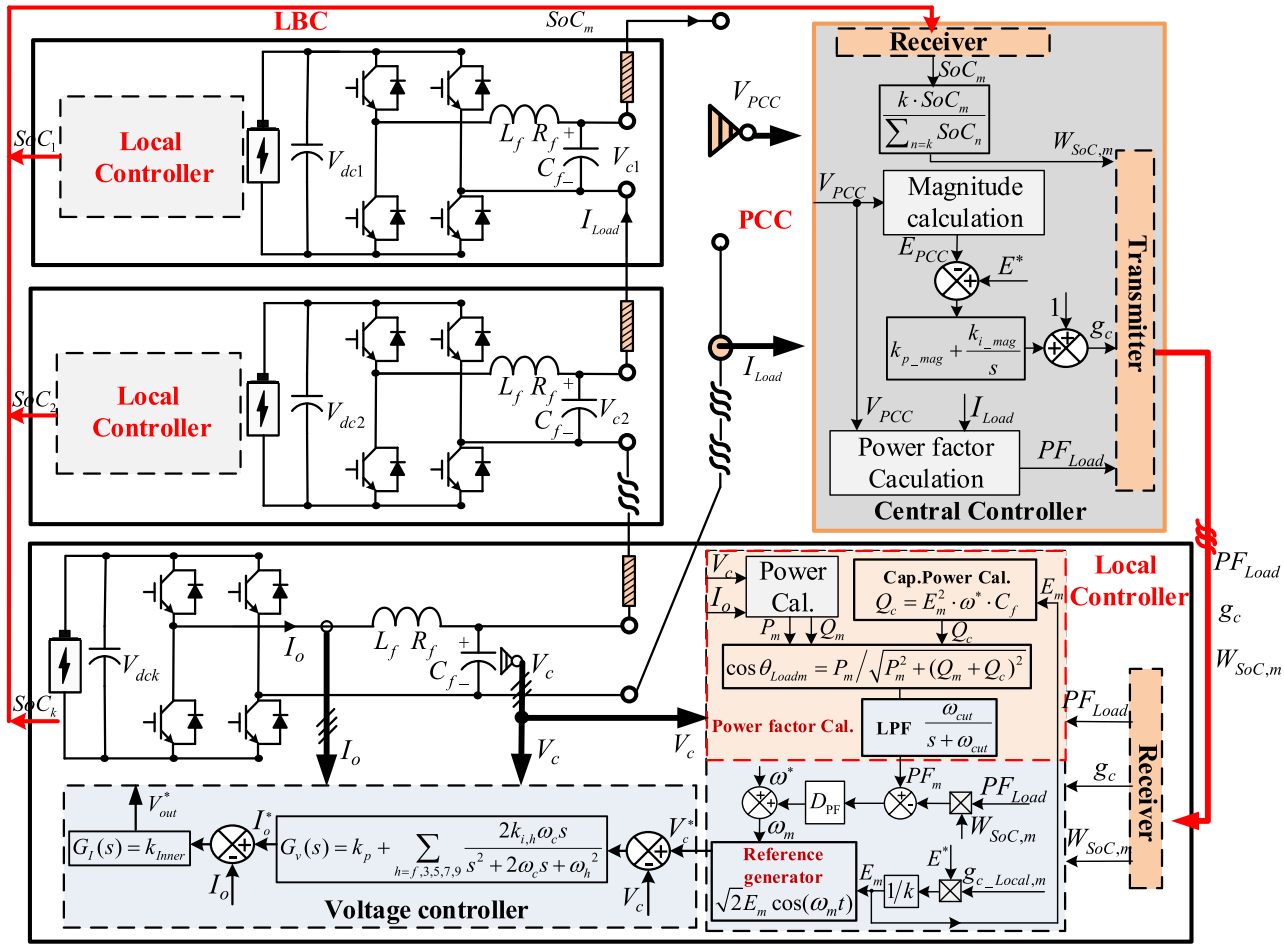

Fig. 2. Diagram of the proposed approach for series-connected power cells-based islanded microgrid.

are sent back to the corresponding local controllers via LBC systems. As it is discussed later, they are used as calibration terms for the flexible proportional power sharing and the frequency deviation suppression through power cell local regulations.

B. Local Control

At an arbitrary power cell local controller m, it receives the coefficients $\boldsymbol{g_c}$, $\boldsymbol{PF_{Load}}$, and $\boldsymbol{W_{SOC}}$, $\boldsymbol{m}$ from the central controller. It is necessary to consider the characteristics of the communication delays in the process of receiving information from PCC. The impact of communication delay is usually modeled by a first-order Pade approximation [26]. In this paper, as the weighted average SoC changes very slowly, only communication delays in receiving the time varying gain $\boldsymbol{g_c}$ are considered in the analysis. Accordingly, the gain at the local controller m is expressed as

$$g_{\mathrm{c\_Local},m} = g_c \cdot G_{\mathrm{delay}}(s) = \frac{1-(\tau_m/2)\,s}{1+(\tau_m/2)\,s} \cdot g_c \tag{3}$$

where $\boldsymbol{\tau_m}$ is the delay time constant of the Pade approximate model. It is apparent that larger $\boldsymbol{\tau_m}$ indicates longer time delay of the LBC.

Afterward, the power sharing among series-connected power cells is realized by the power cell local voltage adjustment strategy. Prior to obtain the instantaneous reference voltage, the reference voltage magnitude $\boldsymbol{E_m}$ and the reference angular frequency $\boldsymbol{\omega_m}$ of power cell m are determined as

$$E_m = \frac{E^*}{k} \cdot g_{\mathrm{c\_Local},m} \tag{4}$$

$$\omega_m = \omega^* + D_{\mathrm{PF}} \cdot (\mathrm{PF}_m - W_{\mathrm{SoC},m} \cdot \mathrm{PF}_{\mathrm{Load}}) \tag{5}$$

where $\boldsymbol{PF_m}$ is power factor of the power cell m, $\boldsymbol{D_{PF}}$ is the inverse droop coefficient, and $\boldsymbol{\omega^*}$ is the nominal angular frequency.

$\boldsymbol{PF_m}$ in (5) is calculated by using only local measurement of H-bridge output current $\boldsymbol{I_o}$ and LC filter capacitor voltage $\boldsymbol{V_c}$, as shown in the bottom of Fig. 2. Note the offset reactive power of the filter capacitor is estimated according to the reference voltage magnitude $\boldsymbol{E_m}$ and then it is deducted from the power factor calculation process. It is also necessary to note that the calculated power factor is filtered by an LPF with cut-off angular frequency $\boldsymbol{\omega_{cut}}$ to avoid power cell power factor jittering caused

by ripples of line current and power cell voltage as

$$\mathrm{PF}_m = \frac{\omega_{\mathrm{cut}}}{s+\omega_{\mathrm{cut}}}\cos(\theta_{\mathrm{Loadm}}) \tag{6}$$

where $\boldsymbol{\theta_{Loadm}}$ is the instantaneous power factor angle of the power cell m.

With (4) and (5), the reference voltage of each power cell $\boldsymbol{V_c^*}$ can be determined by a sinusoidal reference voltage signal generator. Then, a well-understood double-loop voltage controller [27]–[29] is adopted by the power cell to ensure an accurate voltage tracking as

$$\begin{aligned} I_o^* &= G_V(s)\cdot(V_c^* - V_c) \\ &= \left(k_p + \sum_{h=f,3,5,7,9,11} \frac{2k_{i,h}\omega_c s}{s^2+2\omega_c s+\omega_h^2}\right)\cdot(V_c^* - V_c) \end{aligned} \tag{7}$$

$$V_{\mathrm{out}}^* = G_I(s)\cdot(I_o^* - I_o) = k_{\mathrm{Inner}}\cdot(I_o^* - I_o) \tag{8}$$

where $\boldsymbol{V_c}$ is the measured power cell voltage, $\boldsymbol{k_p}$ is the proportional gain, $\boldsymbol{k_{i,h}}$ is the resonant controller gain at the fundamental or harmonic order $\boldsymbol{h}$, $\boldsymbol{\omega_c}$ is the angular bandwidth of a quasi-resonant controller, $\boldsymbol{\omega_h}$ is the angular frequency of controller at order $\boldsymbol{h}$, $\boldsymbol{k_{Inner}}$ is the proportional gain of the inner loop controller, $\boldsymbol{I_o}$ is the measured interfacing converter output current, $\boldsymbol{I_o^*}$ is the reference current of the inner loop, and $\boldsymbol{V_{out}^*}$ is the reference voltage for PWM processing. Note that the bandwidth of the closed-loop voltage and current tracking is much higher than the power sharing loop using inverse droop control. Accordingly, the parameters of a double-loop controller are designed without considering power control conditions and they are usually realized via an iterative process [29].

The completed control diagram of the proposed islanded system is shown in Fig. 2, where it is seen that the central controller collects the SoCs of all batteries of the power cells. Then, the weighted average SoC $\boldsymbol{W_{SOC,m}}$ of each power cell and the PCC load power factor $\boldsymbol{PF_{Load}}$ are determined at the central controller. Meanwhile, the PCC voltage magnitude gain $\boldsymbol{g_c}$ is obtained via a simple magnitude regulator. These data are sent back to all power cell local controllers via the LBC system. In addition, the demonstration of a power cell local controller is provided at the bottom of the figure. First, the receiver of the local controller obtains the status information from the central controller. Then, the reference voltage is determined by (4) and (5) to ensure an accurate power sharing in proportion to the corresponding battery SoC and the mitigation of PCC voltage magnitude and frequency deviations. Finally, a double-loop voltage controller is adopted to obtain a rapid tracking of power cell output *LC* filter capacitor voltage.

III. Analysis and Discussion

This section starts with the performance comparison between the proposed method and conventional methods. Then, the parameter selection guideline of the proposed control method is given via the small-signal analysis. Finally, the potential applications of the proposed system and the interactions with conventional microgrid components are presented.

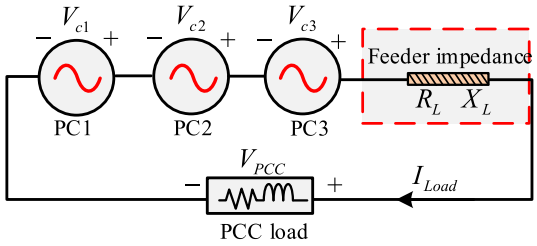

Fig. 3. Equivalent circuit of the series-connected power cells-based islanded microgrid.

A. Phasor Diagram

The equivalent circuit of the string converters-based islanded microgrid is shown in Fig. 3. Considering that the bandwidth of power cell closed-loop voltage tracking is sufficiently higher than the dynamics of power sharing via inverse power factor droop control, three power cells can be modeled as ideal controlled voltage sources as $\boldsymbol{V_{c1}}$, $\boldsymbol{V_{c2}}$, and $\boldsymbol{V_{c3}}$, respectively. The distributed connection wires are lumped as a single feeder as $\boldsymbol{R_L}$ and $\boldsymbol{X_L}$, where $\boldsymbol{R_L}$ is the equivalent resistance and $\boldsymbol{X_L}$ is the equivalent reactance.

Under various situations, the phasor diagrams of the system are sketched in Fig. 4, where the reference frame is aligned to the load current phasor in the horizontal direction. First, when no active power sharing control is applied to the system, the corresponding phasor diagram is shown in Fig. 4(a). It illustrates that each power cell has fixed voltage magnitude at $\boldsymbol{E^*/k}$. However, due to a fact of random phase angles and nontrivial voltage drops on the feeders resistance as $\boldsymbol{R_L I_{Load}}$ and reactance as $\boldsymbol{X_L I_{Load}}$, it is seen that the magnitude of PCC voltage $\boldsymbol{E_{PCC}}$ is significantly lower than the nominal voltage at $\boldsymbol{E^*}$. Here, the nominal voltage magnitude is descripted as the boundary of dashed outer circle.

On the other hand, the phasor diagram of the system using the fully decentralized inverse droop controller [21] is provided in Fig. 4(b). It can be seen that the power cell voltage $\boldsymbol{V_{c1}}$, $\boldsymbol{V_{c2}}$, and $\boldsymbol{V_{c3}}$ have the same phase angle under the steady-state operation condition. In this case, the sum of power cell voltage magnitudes is the same as the nominal PCC voltage. Nevertheless, as there are nontrivial voltage drops on the lumped feeder, the PCC voltage magnitude is still less than the nominal value $\boldsymbol{E^*}$.

The performance using the proposed approach is also shown in Fig. 4(c). In this case, the power cell voltage phase angles are not the same due to the difference of the weighted average SoC of power cells. In this case, the projection of power cell voltage vectors at the horizontal direction is in proportion to output real power of the corresponding power cell. As mentioned earlier, the voltage phase difference of the power cells can further aggravate the magnitude deviations of PCC voltage. To solve this problem, a voltage magnitude compensation term $\boldsymbol{(g_c - 1)\cdot(E^*/k)}$ is

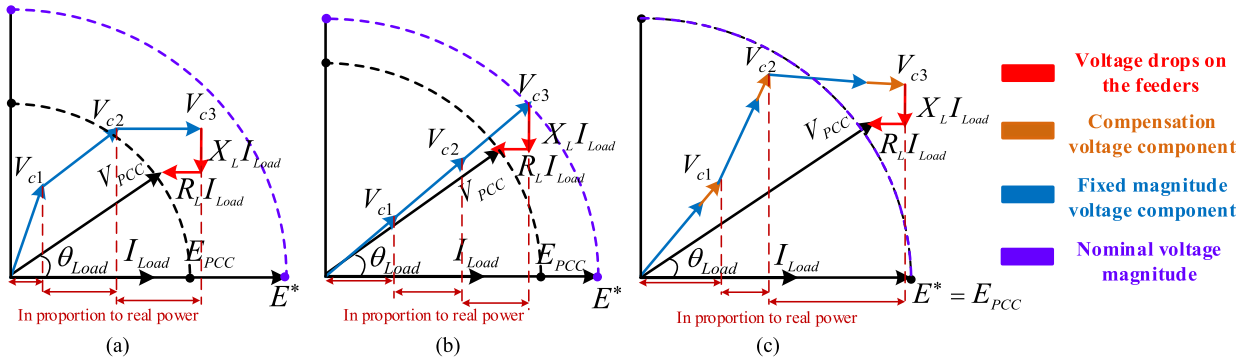

Fig. 4. Phasor diagram of islanded microgrid with different types of control approach. (a) No active control. (b) Inverse droop. (c) Heretical control.

adopted to adjust the voltage magnitude of each power cell. In this figure, the fixed magnitude voltage component and the compensation voltage component are highlighted by blue and saffron yellow vectors, respectively. With the application of the adjustable gain $\boldsymbol{g_c}$, an accurate PCC voltage vector control at nominal magnitude can always be obtained even under the case of unequal real power sharing and there are nontrivial voltage drops on the feeders.

It is easy to understand that the PCC voltage magnitude $\boldsymbol{E_{PCC}}$ can be controlled at the nominal values at the steady state, as active control in (1) is applied. Nevertheless, understanding the performance of PCC voltage frequency restoration is not straightforward. In the following paragraphs, the PCC voltage frequency performances under various cases are discussed.

First, it is a fact that all power cells frequencies and PCC voltage frequency are the same at a steady state, as long as they are synchronized. Supposing the system has a small angular frequency deviation at the steady state, it can be given as

$$\omega_1 = \omega_2 = \cdots = \omega_k = \omega^* + \Delta\omega \tag{9}$$

where $\boldsymbol{\omega_1}$ to $\boldsymbol{\omega_k}$ are the power cell frequencies and $\boldsymbol{\Delta\omega}$ is static angular frequency deviation.

It is necessary to note that power cell reference frequencies are actually determined by their inverse droop controllers as

$$\begin{aligned} \omega_1 &= \omega^* + D_{\mathrm{PF}} \cdot (\mathrm{PF}_1 - W_{\mathrm{SoC},1} \cdot \mathrm{PF}_{\mathrm{Load}}) = \omega^* + \Delta\omega \\ \omega_2 &= \omega^* + D_{\mathrm{PF}} \cdot (\mathrm{PF}_2 - W_{\mathrm{SoC},2} \cdot \mathrm{PF}_{\mathrm{Load}}) = \omega^* + \Delta\omega \\ &\cdots \end{aligned} \tag{10}$$

When combining the above equations together and considering the relationship in (2), the static angular frequency deviation using the proposed approach can be determined as

$$\Delta\omega = D_{\mathrm{PF}} \cdot \left(\frac{1}{k} \cdot \sum_{m=1,2,\ldots k} \mathrm{PF}_m - \mathrm{PF}_{\mathrm{Load}} \right). \tag{11}$$

This actually indicates that when the arithmetic mean value of power cell power factors is not equal to the load power factor, there is some static frequency deviation. In addition, this frequency deviation is proportional to the inverse droop gain $\boldsymbol{D_{\mathrm{PF}}}$. Considering that the series-connected power cells always have the same output apparent power but the power factors are not the same due to different values of battery SoCs, the angular frequency deviation $\boldsymbol{\Delta\omega}$ under the case of varying battery states and PCC load power factors shall be examined.

It is necessary to note that, for practice, the battery SoCs should be controlled to not have significant differences. In this paper, the analysis is conducted in a condition with three series-connected power cells and the SoC1 and SoC2 are the same at 90%, while the SoC3 range is restricted from 80% to 100%. The angular frequency deviation $\boldsymbol{\Delta\omega}$ under the case of different PCC load power factors is shown in Fig. 5(a). It is interesting to note that the angular frequency deviation is zero when the SoC3 is equal to SoC1 and SoC2 at 90%. However, the angular frequency deviation is larger when SoC3 is far away from 90% and it is up to 0.075 rad/s when the SoC3 is 100% with the given inverse droop gain $\boldsymbol{D_{\mathrm{PF}}}$ at 12 rad/s. In addition, higher PCC load power factor is associated with higher frequency deviation.

On the other hand, it is known that for the equal power sharing using the conventional approach in [21], the power cell output power factor is always equal to the load power factor. In this case, the frequency deviation is simply determined by the inverse power factor droop control at $\boldsymbol{D_{\mathrm{PF}} PF_{Load}}$. For a system with the same inverse droop gain at 12 rad/s and a varying PCC load power factor from 0.6 to 0.9, the comparison of PCC frequency deviation performance is illustrated in Fig. 5(b). It is clearly seen that the conventional method induces significant angular frequency errors up to 10.8 rad/s, while the proposed method gives small angular frequency error range that is no more than 0.075 rad/s.

B. Small-Signal Modeling

In order to further investigate the stability and the damping performance of the series-connected power cells-based islanded microgrid system, the corresponding small-signal model for a system with three power cells is established and the detailed validation is conducted by root-loci analysis [30].

First, assuming the PCC voltage with the instantaneous phase angle $\boldsymbol{\theta_{V_{pcc}}}$ is aligned to the horizontal direction in the synchronous rotating reference frame. In this case, the relative voltage phase angle of each power cell in this rotating reference frame is expressed as $\boldsymbol{\theta_i}$ (i = 1, 2, and 3). Then, the detailed system phasor diagram is shown in Fig. 6, where the relative

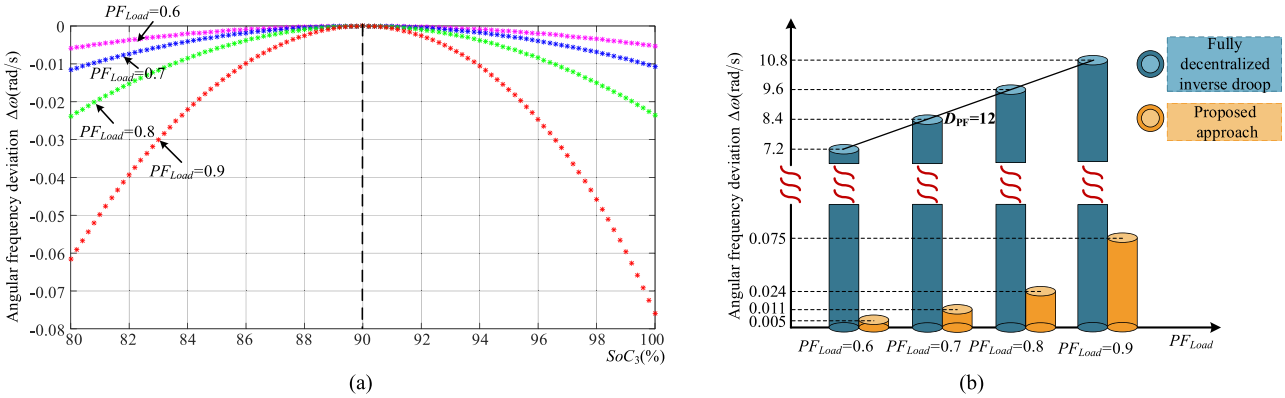

Fig. 5. Analysis of angular frequency deviations. (a) Performance of the proposed islanded microgrid with varying SoC_3 but fixed $SoC_1 = 90\%$ and $SoC_2 = 90\%$. (b) Comparison of angular frequency deviations under different control strategies. Proposed approach with fixed SoC1 = 90%, SoC2 = 90%, and SoC3=100%.

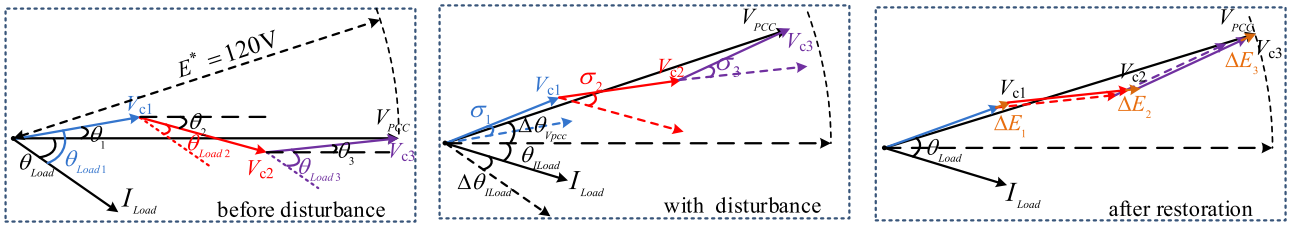

Fig. 6. Phasor diagram of series-connected power cells system with small-signal phase angle disturbance.

load current phasor is $\boldsymbol{\theta_{Load}}$ lagging of PCC voltage phasor. In addition, the phase differences between power cell voltages and load current are $\boldsymbol{\theta_{Load}}_1$, $\boldsymbol{\theta_{Load}}_2$, and $\boldsymbol{\theta_{Load}}_3$, respectively.

Assuming that power cells have small phase angles disturbance as $\boldsymbol{\sigma}_1$, $\boldsymbol{\sigma}_2$, and $\boldsymbol{\sigma}_3$ but the voltage magnitudes of power cells are fixed, the variation of PCC voltage phase angle $\boldsymbol{\Delta\theta_{Vpcc}}$ is obtained as

$$\Delta\theta_{V\mathrm{pcc}} = \sum_{m=1,2,3} C_{\theta V,m} \cdot \sigma_m \tag{12}$$

where $\boldsymbol{\Delta}$ means small disturbance at the equilibrium point and $\boldsymbol{C_{\theta V,m}}$ is an intermediate coefficient that includes static system operation point information as

$$C_{\theta V,m} = \frac{\cos(\theta_m)\cdot\sum_{i=1,2,3}\cos(\theta_i) + \sin(\theta_m)\cdot\sum_{i=1,2,3}\sin(\theta_i)}{\left(1+\left(\frac{\sum_{i=1,2,3}\sin(\theta_i)}{\sum_{i=1,2,3}\cos(\theta_i)}\right)^2\right)\cdot\left(\sum_{i=1,2,3}\cos(\theta_i)\right)^2}. \tag{13}$$

Considering that the PCC load power factor is constant during this short period of the transient voltage regulation process, the load current $\boldsymbol{I_{Load}}$ phasor also has the same phase angle variation $\boldsymbol{\Delta\theta_{ILoad}}$ as the PCC voltage phasor. This simply yields

$$\Delta\theta_{V\mathrm{pcc}} = \Delta\theta_{I\mathrm{Load}}. \tag{14}$$

Then, for an arbitrary power cell m, the variations of power factor angle and measured power factor for inverse droop control are expressed as

$$\Delta\theta_{\mathrm{Loadm}} = \sigma_m - \Delta\theta_{I\mathrm{Load}} = \sigma_m - \sum_{m=1,2,3} C_{\theta V,m}\cdot\sigma_m \tag{15}$$

$$\Delta\mathrm{PF}_m = \frac{\omega_{\mathrm{cut}}}{s+\omega_{\mathrm{cut}}}[\cos(\theta_{\mathrm{Loadm}}+\Delta\theta_{\mathrm{Loadm}}) - \cos(\theta_{\mathrm{Loadm}})]$$

$$= \frac{-\omega_{\mathrm{cut}}}{s+\omega_{\mathrm{cut}}}\sin(\theta_{\mathrm{Loadm}})\left[\sigma_m - \sum_{m=1,2,3} C_{\theta V,m}\cdot\sigma_m\right]. \tag{16}$$

When there is a change of measured power cell power factor as shown above in (16), the inverse droop control in (5) takes action and the corresponding small signal equation is expressed as

$$\Delta\omega_m = D_{\mathrm{PF}}\cdot\Delta\mathrm{PF}_m. \tag{17}$$

It is easy to know that $\boldsymbol{\sigma_m} = (1/s)\cdot\boldsymbol{\Delta\omega_m}$ and by using similar analytical approach in (12)–(17) to all power cells, the angle response of the system can be evaluated using the following closed-loop matrix equation as shown (18), which is provided in the bottom of the next page.

It is necessary to note that the magnitude regulation also happens at the same time. However, the magnitude control only has very minor impact of the angles control, as power cell power factor is very well decoupled with its slight voltage magnitude regulation. Thus, it is applicable to determine the magnitude response independently. For this series-connected power cells-based microgrid, the feeder impedance can be considered as a part of the load for the sake simplicity. Accordingly, the voltage

magnitude of PCC is approximately expressed as

$$E_{\mathrm{PCC}} = \left(\left(\sum_{i=1,2,3} E\cos\left(\theta_i\right) \right)^2 + \left(\sum_{i=1,2,3} E\sin\left(\theta_i\right) \right)^2 \right)^{\frac{1}{2}} \tag{19}$$

where E is voltage magnitude of each power cell at the static working point. After small phase angles disturbances as $\boldsymbol{\sigma}_1$, $\boldsymbol{\sigma}_2$, and $\boldsymbol{\sigma}_3$, the variation of PCC voltage magnitude is expressed as

$$\Delta E_{PCC} = \sum_{m=1,2,3} C_{E\theta,m} \cdot \sigma_m + \sum_{m=1,2,3} C_{EE,m} \cdot \Delta E_m \tag{20}$$

where $\boldsymbol{C_{E\theta,m}}$ and $\boldsymbol{C_{EE,m}}$ are intermediate coefficients that include the system static working point information as

$$C_{E\theta,m} = \frac{E^2}{E_{\mathrm{PCC}}} \left(\cos\left(\theta_m\right) \sum_{i=1,2,3} \sin\left(\theta_i\right) - \sin\left(\theta_m\right) \sum_{i=1,2,3} \cos\left(\theta_i\right) \right) \tag{21}$$

$$C_{EE,m} = \frac{E}{E_{\mathrm{PCC}}} \left(\cos\left(\theta_m\right) \sum_{i=1,2,3} \cos\left(\theta_i\right) + \sin\left(\theta_m\right) \sum_{i=1,2,3} \sin\left(\theta_i\right) \right). \tag{22}$$

When the variation of PCC voltage magnitude is detected by the central controller, the restoration controller in (1) takes effect and the gain is transmitted to the power cell local controller. According to (1) and (3) with proper considerations of communication delay, the change of the gain $\boldsymbol{\Delta g_{c\_Local,m}}$ at the local controller m is descripted as

$$\Delta g_{c\_\mathrm{Local},m} = -\Delta E_{\mathrm{PCC}} \cdot \left(k_{p\_\mathrm{mag}} + \frac{k_{i\_\mathrm{mag}}}{s} \right) \cdot \left(\frac{1 - (\tau_m/2)\, s}{1 + (\tau_m/2)\, s} \right). \tag{23}$$

Accordingly, the variation of power cell m voltage magnitude is

$$\Delta E_m = \frac{E^*}{k} \cdot \Delta g_{c\_\mathrm{Local},m}. \tag{24}$$

By applying a similar analytical approach in (19)–(24) to all series string converters, the small signal response of the system caused by voltage magnitude regulation can be determined as (25) shown at the bottom of this page.

It can be seen that the components in the diagonal line are second-order transfer functions that indicate the magnitude response of a power cell to the system voltage magnitude and phase angle disturbances. In contrast to the previous matrix in (18), it is interesting to indicate that both the angle disturbances and the magnitude disturbances have impact of PCC voltage magnitude, and therefore, the proposed magnitude controller takes action. The magnitude control performances of a system with three series power cells are shown from Figs. 7 to 8, where the power

$$\begin{bmatrix} s^2 + \omega_{\mathrm{cut}} s + (\omega_{\mathrm{cut}} D_{\mathrm{PF}} \sin(\theta_{\mathrm{Load1}}))(1 - C_{\theta V,1}) & -C_{\theta V,2}\omega_{\mathrm{cut}} D_{\mathrm{PF}} \sin(\theta_{\mathrm{Load1}}) & -C_{\theta V,3}\omega_{\mathrm{cut}} D_{\mathrm{PF}} \sin(\theta_{\mathrm{Load1}}) \\ -C_{\theta V,1}\omega_{\mathrm{cut}} D_{\mathrm{PF}} \sin(\theta_{\mathrm{Load2}}) & s^2 + \omega_{\mathrm{cut}} s + (\omega_{\mathrm{cut}} D_{\mathrm{PF}} \sin(\theta_{\mathrm{Load2}}))(1 - C_{\theta V,2}) & -C_{\theta V,3}\omega_{\mathrm{cut}} D_{\mathrm{PF}} \sin(\theta_{\mathrm{Load2}}) \\ -C_{\theta V,1}\omega_{\mathrm{cut}} D_{\mathrm{PF}} \sin(\theta_{\mathrm{Load3}}) & -C_{\theta V,2}\omega_{\mathrm{cut}} D_{\mathrm{PF}} \sin(\theta_{\mathrm{Load3}}) & s^2 + \omega_{\mathrm{cut}} s + (\omega_{\mathrm{cut}} D_{\mathrm{PF}} \sin(\theta_{\mathrm{Load3}}))(1 - C_{\theta V,3}) \end{bmatrix} \cdot \begin{bmatrix} \sigma_1 \\ \sigma_2 \\ \sigma_3 \end{bmatrix} = 0 \tag{18}$$

$$\begin{bmatrix} a_{11} & 0 & 0 & 0 & 0 & 0 \\ 0 & a_{12} & 0 & 0 & 0 & 0 \\ 0 & 0 & a_{13} & 0 & 0 & 0 \\ 0 & 0 & 0 & a_{14} & 0 & 0 \\ 0 & 0 & 0 & 0 & a_{15} & 0 \\ 0 & 0 & 0 & 0 & 0 & a_{16} \end{bmatrix} \cdot \begin{bmatrix} \sigma_1 \\ \sigma_2 \\ \sigma_3 \\ \Delta E_1 \\ \Delta E_2 \\ \Delta E_3 \end{bmatrix}$$

$$= 0 \begin{cases} a_{11} = \left(E^* k_{p\_\mathrm{mag}} C_{E\theta,1}/k\right) s + E^* k_{i\_\mathrm{mag}} C_{E\theta,1}/k \\ a_{12} = \left(E^* k_{p\_\mathrm{mag}} C_{E\theta,2}/k\right) s + E^* k_{i\_\mathrm{mag}} C_{E\theta,2}/k \\ a_{13} = \left(E^* k_{p\_\mathrm{mag}} C_{E\theta,3}/k\right) s + E^* k_{i\_\mathrm{mag}} C_{E\theta,3}/k \\ a_{14} = \left(\frac{\tau_1}{2} + \frac{\tau_1^2}{4} E^* k_{p\_\mathrm{mag}} C_{EE,1}/k\right) s^2 + \left(1 - \left(k_{p\_\mathrm{mag}} - \frac{\tau_1}{2} k_{i\_\mathrm{mag}}\right) E^* C_{EE,1}/k\right) s - E^* k_{i\_\mathrm{mag}} C_{EE,1}/k \\ a_{15} = \left(\frac{\tau_2}{2} + \frac{\tau_2^2}{4} E^* k_{p\_\mathrm{mag}} C_{EE,2}/k\right) s^2 + \left(1 - \left(k_{p\_\mathrm{mag}} - \frac{\tau_2}{2} k_{i\_\mathrm{mag}}\right) E^* C_{EE,2}/k\right) s - E^* k_{i\_\mathrm{mag}} C_{EE,2}/k \\ a_{16} = \left(\frac{\tau_3}{2} + \frac{\tau_3^2}{4} E^* k_{p\_\mathrm{mag}} C_{EE,3}/k\right) s^2 + \left(1 - \left(k_{p\_\mathrm{mag}} - \frac{\tau_3}{2} k_{i\_\mathrm{mag}}\right) E^* C_{EE,3}/k\right) s - E^* k_{i\_\mathrm{mag}} C_{EE,3}/k \end{cases} \tag{25}$$

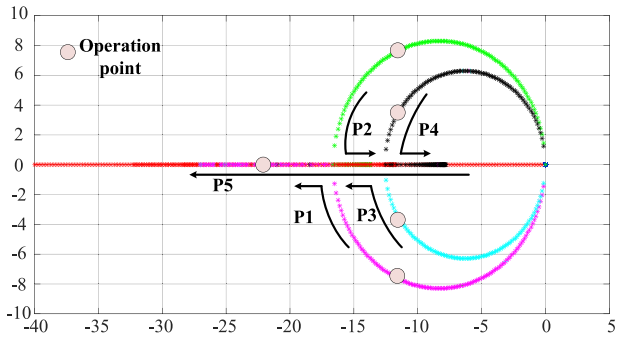

Fig. 7. Root locus diagram of phase angle response when the LPF cut-off angular frequency $\omega_{\rm cut}$ changes from 1 to 37 rad/s while $D_{\rm PF}$ is fixed to 12 rad/s.

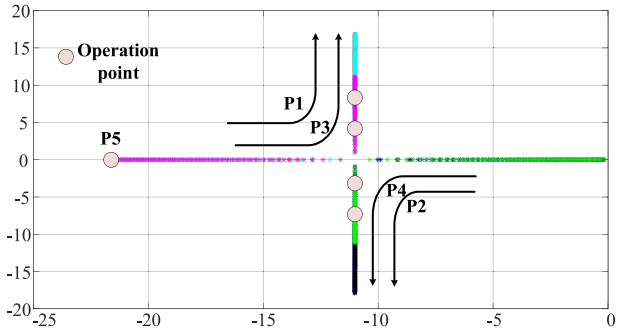

Fig. 8. Root locus diagram of phase angle response when the inverse droop coefficient $D_{\rm PF}$ changes from 0.5 to 40 rad/s while $\omega_{\rm cut}$ is fixed to 15 rad/s.

TABLE I
PARAMETERS OF THE EXPERIMENTAL SYSTEM

Circuit Parameter	Value
Rated voltage	Single-phase 120 V/60 Hz
DC link capacitor	C_{DC}=2000 μF
LC filter	L_f=1 mH ; C_f=20 μF
DC link voltage	85 V
Series Power cell number	3
Control parameter	**Value**
Switching frequency	5 kHz
Dead-time	2.5 μsec
Low-pass angular frequency	15 rad/s
k_{p_mag}	0.15/V
k_{i_mag}	0.006/(V · s)
k_p	0.3 A/V
$k_{i,h}$	35 A/(V · s),h=1; 25 A/(V · s),h=3
$D_{\rm PF}$	12 rad/s
ω_{cut}	15 rad/s
k_{Inner}	25 V/A

circuit parameters are chosen to be the same as in the experiment as shown in Table I. In order to emulate the impact of communication delays, the delay time constant $\boldsymbol{\tau_m}$ for power cells are intentionally set up to be large. In addition, it is set to be slightly different for three power cells at 0.01, 0.011, and 0.012 s, respectively.

First, Fig. 7 shows the frequency control performance of the system when the inverse droop coefficient $\boldsymbol{D_{\rm PF}}$ is fixed while

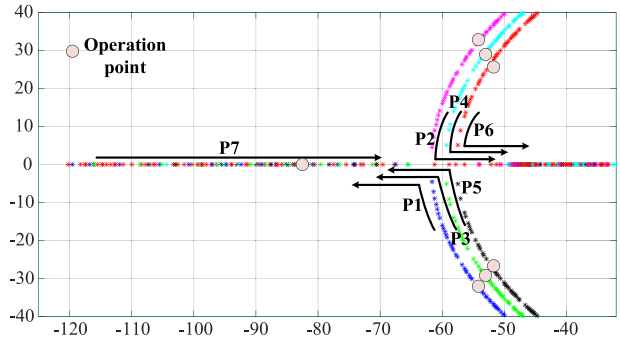

Fig. 9. Root locus diagram of magnitude response when the proportional gain of the PI regulator $k_{p\_\rm mag}$ changes from 0.01/V to 0.4/V while $k_{i\_\rm mag}$ is fixed to 0.006/(V·s).

the cut-off angular frequency $\boldsymbol{\omega_{cut}}$ of the low-pass filter in (6) for power cell power factor calculation increases from 1 to 37 rad/s. When the cut-off angular frequency is small, all poles are close to the imaginary axis of the map. This means a reduced stability margin and a slow response after small signal disturbances. When the cut-off angular frequency increases, all poles move away from the imaginary axis in the beginning of the process, indicating better stability margining. It also is interesting to find that P1–P4 become less dampened in the middle of the specified $\boldsymbol{\omega_{cut}}$ variation range. By further increasing $\boldsymbol{\omega_{cut}}$, P1 and P3 keep moving away from the imaginary axis and they eventually become no-dominated poles. At the same time, P2, P4, and P5 are pushed back to the imaginary axis, leading to less stability margin. To get a tradeoff between proper stability margin and damping performance, the cut-off angular frequency of the system is selected as 15 rad/s.

On the other hand, when the cut-off angular frequency is fixed to 15 rad/s but the inverse droop coefficient $\boldsymbol{D_{\rm PF}}$ increases from 0.5 to 40 rad/s, the performance of the system is shown in Fig. 8. In this case, the system has four moving poles P1–P4 of which the position of P5 is mainly fixed. When the inverse droop gain coefficient is small, poles P2 and P4 are located in the real axis and they are very close to the imaginary axis. At the same time, P1, P3, and P5 are also in the real axis but they are far away from the imaginary axis. By increasing the inverse droop coefficient, P2 and P4 move to the left direction but P1 and P3 toward to origin of the plane. However, further increase of gain $\boldsymbol{D_{\rm PF}}$ pushes these poles away from the real axis and the system can be less dampened when the gain is sufficiently large. To have good stability margin and proper damping performance, the inverse droop coefficient $\boldsymbol{D_{\rm PF}}$ is selected as 12 rad/s.

The impacts of the restoration control parameters $\boldsymbol{k_{p\_mag}}$ and $\boldsymbol{k_{i\_mag}}$ to the PCC voltage magnitude response are also investigated as shown in Figs. 9 and 10. First, Fig. 9 shows the system performance when $\boldsymbol{k_{p\_mag}}$ changes from 0.01/V to 0.4/V, while $\boldsymbol{k_{i\_mag}}$ is fixed to 0.006/(V·s). In this analysis, the system has seven valid poles. A trend is that very small gain $\boldsymbol{k_{p\_mag}}$ is associated with less dampened poles P1–P6 and they also have small stability margin. On the other hand, these poles P1–P6 become overdamped when the gain keep increasing. However, it is also seen that P2, P4, and P4 move to the origin of the map when this

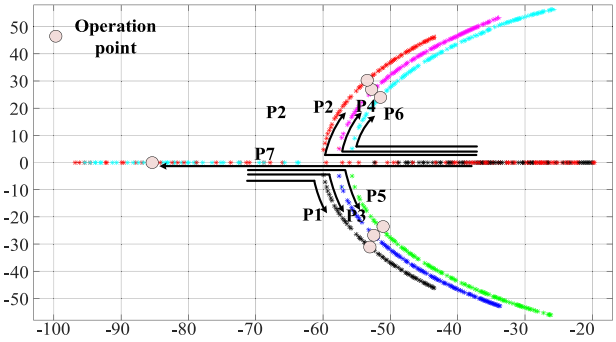

Fig. 10. Root locus diagram of magnitude response when the integral gain of the PI regulator k_{i_mag} changes from 0.001/(V·s) to 0.02/(V·s) while k_{p_mag} is fixed to 0.15/V.

gain is too large. By using similar parameter section rule considering a proper tradeoff between system damping performance and stability margin, $\boldsymbol{k_{p\_mag}}$ is selected as 0.15/V.

Finally, we also investigate the pole positions of the system with varying gain $\boldsymbol{k_{i\_mag}}$ in Fig. 10. When the gain is small, the system is over dampened and it has small stability margin as P2, P4, and P6 are close to origin. On the other hand, the system becomes less dampened when the gain keeps increasing, but poles P1–P6 become too close to imaginary axis. In this paper, $\boldsymbol{k_{i\_mag}}$ is selected as 0.006/(V·s).

From the above detailed small-signal modeling and analysis, it can be concluded that even significant time delays in the communication are considered, the system can still preserve a good stability and damping performance with proper selection of control parameters.

C. Design Requirement and Applications

It has been well accepted that parallel DG units-based microgrid has the capability to interconnect multiple dc sources, as sketched in Fig. 11(a). The power sharing between them can be achieved in a coordinated manner without any communications between parallel DG units interfacing converters, such as using the well understood droop control.

On the other hand, the proposed system can interconnect the same dc sources and loads, but by using a different configuration of power electronic circuits, as shown in Fig. 11(b). Due to a fact that the power circuit configurations are not the same, the conventional droop control for parallel DG units cannot be used. However, from the perspective of source energy generation and load energy consumption, the above two systems have similar functionality only the internal power electronic circuit configuration and control algorithms are different.

Due to unique feature of the proposed system, a few design considerations are briefly mentioned here.

1) Power Cell Number Design Considerations: As dc-bus voltage of power cell is lower than the peak value of rated ac voltage, multiple power cells shall be connected in series. Similar to constrain of conventional CHB converters, a simple constrain for the proposed system is that sum of the dc voltages must be higher than the peak ac voltage

$$\lambda = \sum_{m} E_{\mathrm{dc},m}/E_{\mathrm{peak}} \geq 1 \tag{26}$$

where $\boldsymbol{E_{dc,m}}$ is the dc rail voltage of power cell m and $\boldsymbol{E_{\mathrm{peak}}}$ is the peak value of ac voltage. For practical applications, it is recommended that the coefficient is at around 1.1–1.2 to ensure sinusoidal modulation of each converter and sufficient freedoms to tune the power sharing ratio between power cells.

It is necessary to note that in the case of only a small number of low voltage dc sources available, the proposed single-stage integration method cannot be directly used. A conventional solution is to adopt two-stage power conversion circuit as shown in Fig. 12(a), where two 24-V dc sources are both boosted to high-voltage 200-V dc sources. Then, both high-voltage dc buses are integrated into the ac system using parallel-connected dc/ac inverters. Note that this system needs to use higher rated voltage components including dc capacitors and power switches. Alternatively, another two-stage power conversion is recommended as shown in Fig. 12(b), where it is seen that two 24-V dc sources are boosted to only 100-V dc sources and then the proposed series connection configuration is adopted for the integration of two 100-V dc buses. It is necessary to note that even with two-stage power conversion in Fig. 12(b), the proposed method still has a few favorable features including the adoption of low-voltage devices and the low step-up dc/dc conversions.

2) Integration With Other Subsystems: It is necessary to note that the proposed system can also be a part of more complex microgrids with both cascaded power cells-based sub-microgrids and parallel DG units, as shown in Fig. 13. In this example system, additional control algorithms such as the conventional droop control and its variants may be installed in the central controller of each cascaded power cells sub-microgrid to manage the power sharing between parallel sub-microgrids. Afterward, the internal power sharing among power cells in each sub-microgrid is obtained by using the proposed approach.

IV. Verifications

Experimental results are obtained from a laboratory test-rig as shown in Fig. 14, where three power cells at the same power rating are connected in series. The detailed circuitry configuration is the same as that in Fig. 1. Due to the limitation of laboratory facilities, the dc sources are constructed by using three-phase diode rectifiers with an isolation matching transformer of each. In this test, the real power, reactive power, and power factor of all power cells are obtained by measuring only H-bridge output current $\boldsymbol{I_o}$ and the filter capacitor voltage $\boldsymbol{V_c}$. The detailed circuitry and control parameters of the system can be seen in Table I.

In order to fully demonstrate the effectiveness of the proposed approach, the experimental test system has four operation stages. In this test, although isolated dc sources are adopted to emulate the batteries, we intentionally set up the virtual SoCs of battery 1 to battery 3 as 60%, 60%, and 80%, respectively, and the ratios are 1: 1: 1.33. At Stage 1, three power cells are controlled with

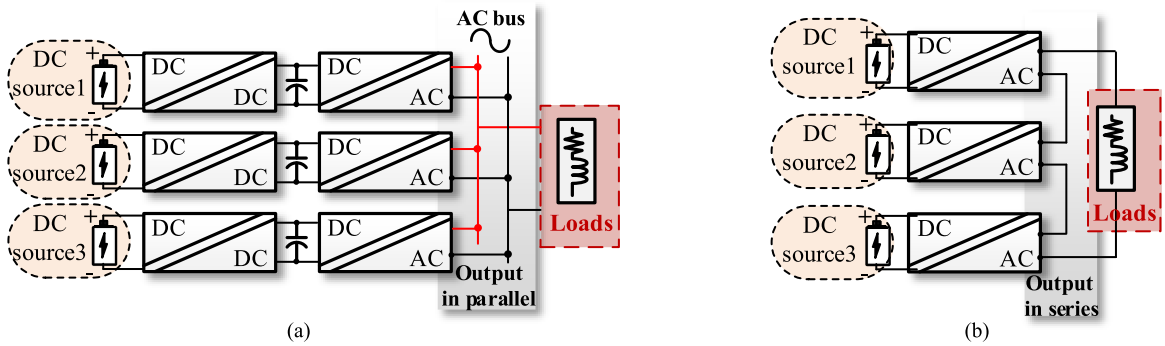

Fig. 11. Comparison of islanded microgrid with different power circuit configuration. (a) Parallel-connected DG units based system. (b) Series-connected power cells based system.

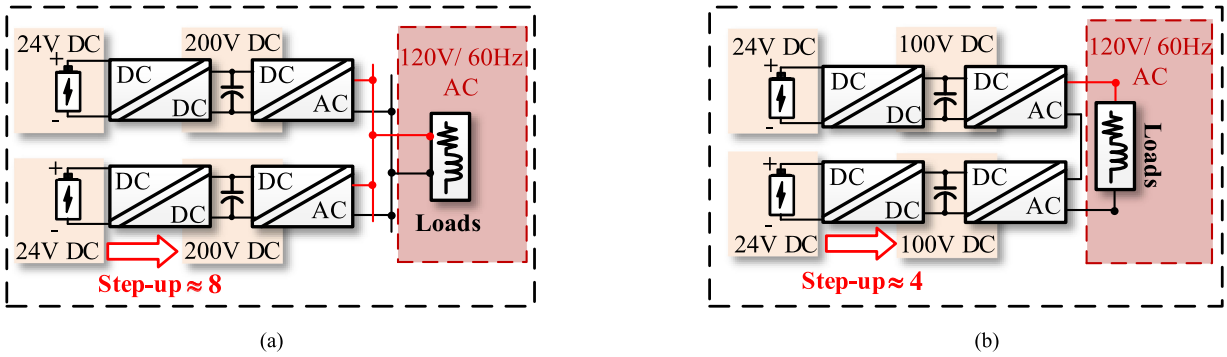

Fig. 12. Two types of two-stage power conversion topology. (a) Parallel-connected DG units with internal dc/dc boost converter. (b) Series-connected power cells with internal dc/dc boost converter.

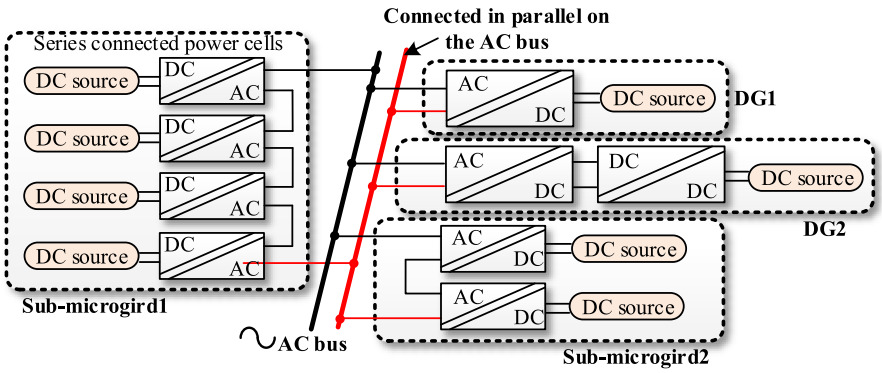

Fig. 13. Diagram of a complex microgrid with series- and parallel-connected power cells.

fixed voltage magnitude and frequency, but the initial phase angles of reference voltages intentionally have 18° displacement. At Stage 2, the fully decentralized inverse power factor droop control is applied to three power cells. At Stage 3, the proposed hierarchical control is applied to the system to obtain real power sharing in proportion to battery SoCs. Finally, there is a sudden PCC load jump at the beginning of Stage 4.

The responses of real power, reactive power, and power factor of all power cells in the entire process are shown in Fig. 15. It is seen that without any active power sharing control, three power cells have different output real and reactive power at Stage 1, as shown in Fig. 15(a) and (b). Note again that we intentionally set 18° initial voltage phase angle differences at Stage 1, in order to emulate a case of independent power cell regulation. Accordingly, at Stage 1, the power factors of three power cells as given in Fig. 15(c) are 0.9, 0.71, and 0.45, respectively.

When the fully decentralized inverse power factor droop control is adopted at Stage 2, it is seen that three power cells have

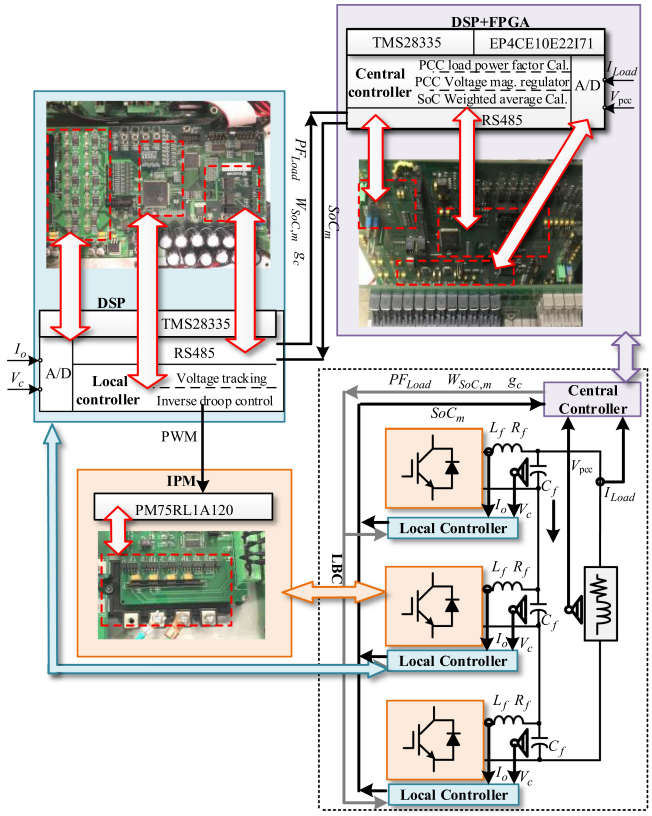

Fig. 14. Detailed demonstration of the experimental test rig.

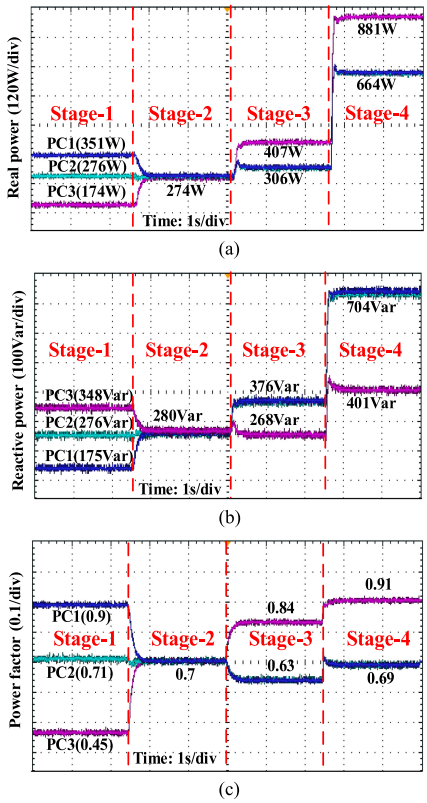

Fig. 15. Real power, reactive power, and power factor performances of power cells.

the same real and reactive power at 274 W and 280 Var, respectively. Accordingly, the power factors of all three power cells change to around 0.7.

At Stage 3, all power cells are designed to have the same output apparent power but the output real power is in proportion to battery SoCs ratios as 1:1:1.333 (for SoC1 = 60%, SoC2 = 60%, and SoC3 = 80%). It is seen that the real power of power cell 1 and power cell 2 increases to 306 W while the real power of power cell 3 increases to 407 W. This real power performance among power cells is clearly very close to the designed ratio as 1:1:1.33. Due to a fact that the apparent power of these power converters is the same, the output reactive power of the three power cells is passively shared at 376, 376, and 268 Var, respectively. At the same time, the power factors of power cells change to 0.63, 0.63, and 0.84, respectively.

Finally, the real power of three power cells jump to 664, 664, and 881 W at Stage 4, when there is a sudden increase of PCC load demand. It is necessary to note that the real power ratios of power cells at Stage 4 are still the same as the corresponding battery SoC ratios as 1:1:1.33, even after the PCC load change. Similar to the performance at Stage 3, the reactive power of power cells at Stage 4 are passively shared at 704, 704, and 401 Var, respectively.

In addition, the gain g_c for PCC voltage magnitude restoration control, the PCC voltage magnitude, the instantaneous frequency of PCC voltage, and all power cell voltages are shown in Fig. 16. It is easy to find that the gain g_c in Fig. 16(a) is

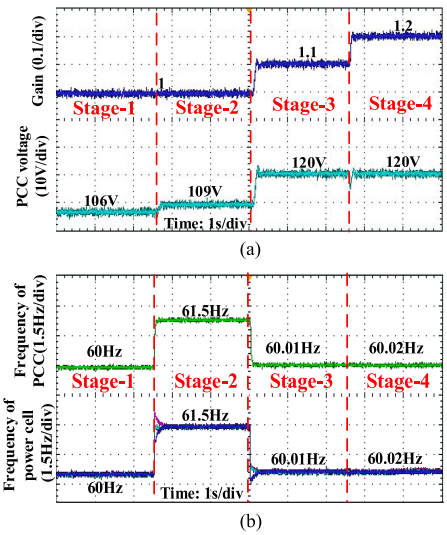

Fig. 16. Gain, frequency, and PCC voltage performances during the process.

fixed to 1 at both Stages 1 and 2. Accordingly, PCC voltage magnitude dips to only 106 and 109 V, respectively. When the proposed hierarchical control is applied to the system to regulate PCC voltage magnitude and frequency, it is seen that the gain g_c slowly increases to around 1.1 at Stage 3 and 1.2 at Stage 4. Due to the involvement of restoration control, the PCC voltage magnitude keeps at 120 V at both Stages 3 and 4, as shown in

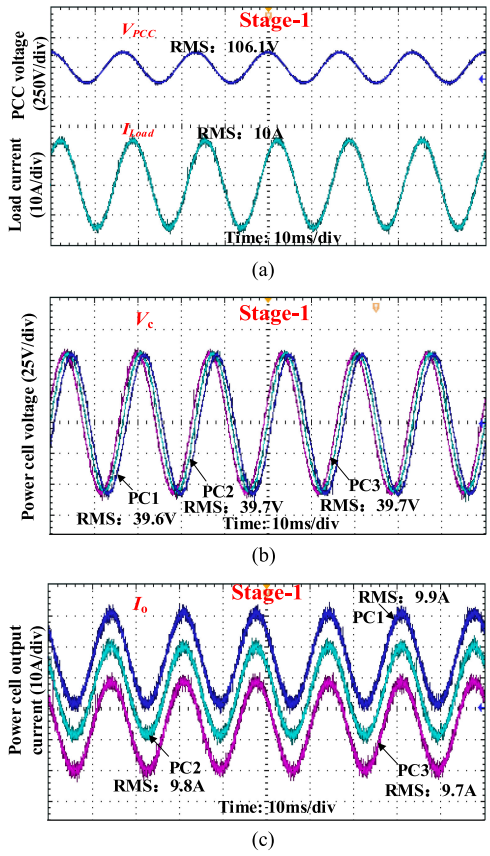

Fig. 17. Detailed voltage and current performances of the system at Stage 1.

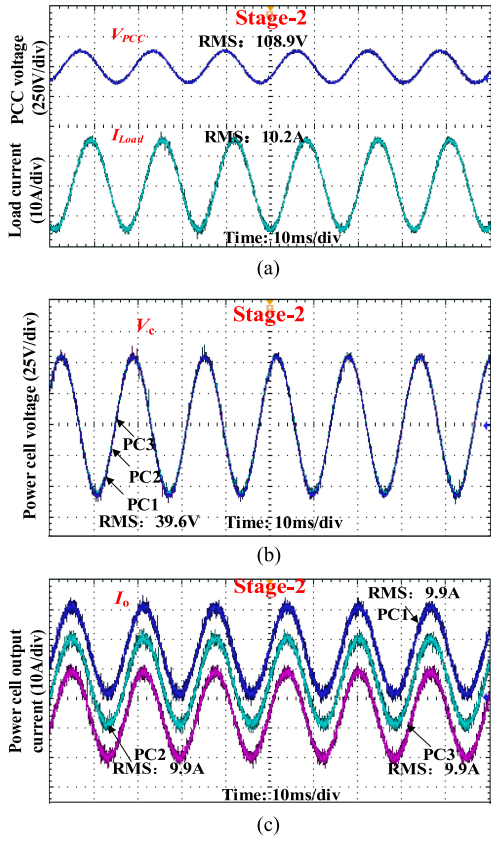

Fig. 18. Detailed voltage and current performances of the system at Stage 2.

the lower part of Fig. 16(a). There is only small transient disturbance during the transfer between Stages 3 and 4 with sudden increase of PCC load demand.

Furthermore, the frequency responses of the system at PCC and all power cells are captured as shown in Fig. 16(b). It is seen that both the power cells and PCC voltage frequencies are fixed to 60 Hz at Stage 1, while they drift to around 61.5 Hz when using the fully decentralized inverse power factor droop control method at Stage 2. Finally, by using the proposed hierarchical control method at Stages 3 and 4, it is seen that both the power cells and the PCC voltage frequencies are almost restored to the nominal value 60 Hz during steady-state operation.

The detailed voltage and current performances of the system at each stage are also provided, as shown from Figs. 17 to 20. First, Fig. 17 shows the PCC voltage, the load current, and the voltage of fours power cells at Stage 1. It is clearly seen from Fig. 17(b) that although all power cells have the same voltage magnitude at around 40 V, the PCC voltage in Fig. 17(a) only has 106 V magnitude due to the phase displacement between power cell voltages and the voltage drops on the distributed feeders.

At Stage 1, the output currents of three string converters are also captured in Fig. 17(c). As three power cells have some voltage phase displacement that affects the filter capacitor current phase angle, it is seen that the output currents of power cells are slightly different even when the power cells are connected in series.

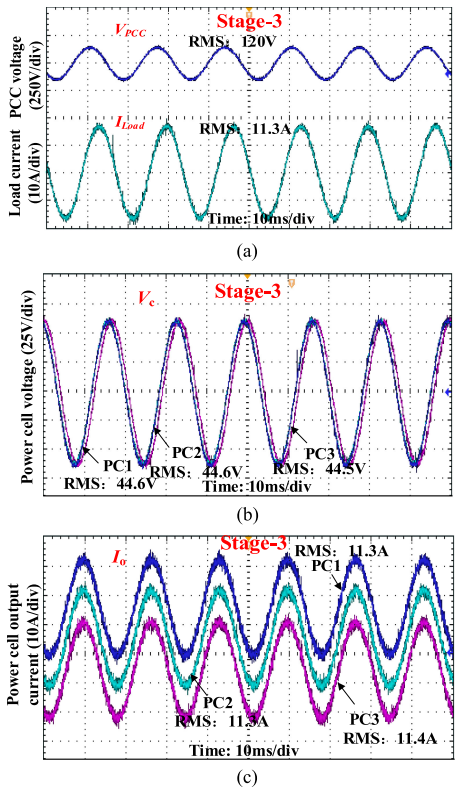

Fig. 19. Detailed voltage and current performances of the system at Stage 3.

TABLE II
PERFORMANCE COMPARISONS

	Stage-1	Stage-2	Stage-3	Stage-4
Power sharing method	No active control	Fully decentralized inverse droop	Hierarchical inverse droop	Hierarchical inverse droop
Communications	No applicable	No applicable	LBC	LBC
Power sharing performance	No power sharing	Equal power sharing only	In proportion to the battery SoCs	In proportion to the battery SoCs
PCC voltage	Significant deviation	Less deviation	Accurate	Accurate
Frequency	Accurate	Significant deviation	Minor deviation	Minor deviation

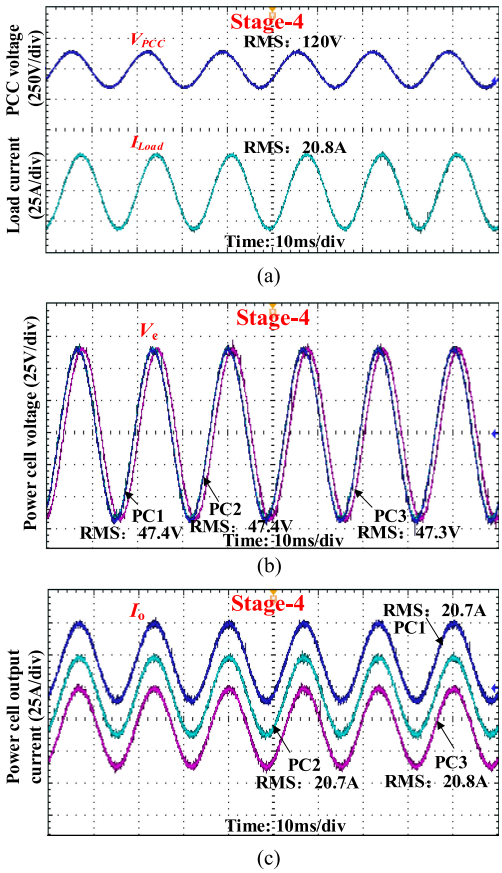

Fig. 20. Detailed voltage and current performances of the system at Stage 4.

When the fully decentralized inverse droop control is applied to the system at Stage 2, it is interesting to find from Fig. 18(b) that three power cell voltages are almost identical and the PCC voltage in Fig. 18(a) increases to 109 V. Note that there are still some PCC voltage magnitude deviations due to the voltage drops on the feeders as illustrated in Fig. 4(b).

As the PCC voltage increases by using inverse power factor droop control at Stage 2, the load current in Fig. 18(a) also slightly increases to 10.2 A. Accordingly, the output currents of three power cells have lower magnitude at 9.9 A.

After the application of the proposed approach at Stage 3, the PCC voltage in the top of Fig. 19(a) is sinusoidal and the magnitude is very accurate at 120 V. However, it is necessary to note that power cells voltage magnitudes and phase angles in Fig. 19(b) are different again due to the requirement of proportional real power sharing according to the corresponding battery bank SoC. Due to the adoption of proportional power sharing, it is found that the power cell output current in Fig. 19(c) is slightly different at 11.3, 11.3, and 11.4 A, respectively.

The steady-state performance of the system after the load jump is presented in Fig. 20. In general, the power cell voltage magnitudes are even higher than the counterparts at Stage 3 in Fig. 19(b), as higher load current causes more voltage drops on the feeders at Stage 4 and it needs to be compensated by power cell voltage magnitude control. It is also interesting to find that the PCC voltage in Fig. 20(a) is still sinusoidal at 120 V. In this test, it is seen that the string converters output currents also increase to 20.7, 20.7, and 20.8 A, respectively.

V. CONCLUSION

This paper has proposed a hierarchical control approach to realize the flexible power sharing among series-connected low-voltage power cells in an autonomous islanded microgrid. An accurate proportional power sharing is achieved by a modified inverse power factor droop using the weighted average SoCs and PCC load power factor information as the dynamic calibration coefficients. In addition, the PCC voltage magnitude deviation is properly mitigated by a secondary restoration controller at PCC central controller. With the coordination between the central and local controllers, the remotely installed low-voltage dc sources can be easily connected in series with single-stage dc/ac power conversion to supply flexible and high-quality power to rated voltage PCC loads, while without any communications among power cell converter local controllers.

Finally, a brief performance comparison of the islanded system using different controllers is provided in Table II, in order to further highlight the superior performance of the proposed hierarchical power sharing approach.

REFERENCES

[1] K. D. Brabandere, B. Bolsens, J. V. D. Keybus, A. Woyte, J. Driesen, and R. Belmans, "A voltage and frequency droop control method for parallel inverters," *IEEE Trans. Power Electron.*, vol. 22, no. 4, pp. 1107–1115, Jul. 2007.

[2] J. M. Guerrero, J. C. Vasquez, J. Matas, L. G. de Vicuna, and M. Castilla, "Hierarchical control of droop-controlled ac and dc microgrids—A general approach toward standardization," *IEEE Trans. Ind. Electron.*, vol. 58, no. 1, pp. 158–172, Jan. 2011.

[3] J. M. Guerrero, J. C. Vasquez, J. Matas, M. Castilla, and L. Garcia de Vicuna, "Control strategy for flexible microgrid based on parallel line-interactive UPS systems," *IEEE Trans. Ind. Electron.*, vol. 56, no. 3, pp. 726–736, Mar. 2009.

[4] J. C. Vasquez, J. M. Guerrero, J. Miret, M. Castilla, and L. G. de Vicuña, "Hierarchical control of intelligent microgrids," *IEEE Ind. Electron. Mag.*, vol. 4, no. 4, pp. 23–29, Dec. 2010.
[5] Y. A. R. I. Mohamed and E. F. El-Saadany, "Adaptive decentralized droop controller to preserve power sharing stability of paralleled inverters in distributed generation microgrids," *IEEE Trans. Power Electron.*, vol. 23, no. 6, pp. 2806–2818, Jun. 2008.
[6] Q.-C. Zhong and G. Weiss, "Synchronverters: Inverters that mimic synchronous generators," *IEEE Trans. Ind. Electron.*, vol. 58, no. 4, pp. 1259–1267, Apr. 2011.
[7] M. Savaghebi, A. Jalilian, J. C. Vasquez, and J. M. Guerrero, "Autonomous voltage unbalance compensation in an islanded droop controlled microgrid," *IEEE Trans. Ind. Electron.*, vol. 60, no. 4, pp. 1390–1402, Apr. 2013.
[8] J. He and Y. W. Li, "An enhanced microgrid load demand sharing strategy," *IEEE Trans. Power Electron.*, vol. 19, no. 5, pp. 1184–1194, May 2014.
[9] Y. Han, H. Li, P. Shen, E. A. A. Coelho, and J. M. Guerrero, "Review of active and reactive power sharing strategies in hierarchical controlled microgrids," *IEEE Trans. Power Electron.*, vol. 32, no. 3, pp. 2427–2451, Mar. 2017.
[10] X. Lu, J. M. Guerrero, K. Sun, and J. C. Vasquez, "An improved droop control method for DC microgrids based on low bandwidth communication with DC bus voltage restoration and enhanced current sharing accuracy," *IEEE Trans. Power Electron.*, vol. 29, no. 4, pp. 1800–1812, Apr. 2014.
[11] J. He, Y. Li, C. Wang, Y. Pan, C. Zhang, and X. Xing, "Hybrid microgrid with parallel- and series-connected microconverters," *IEEE Trans. Power Electron.*, vol. 33, no. 6, pp. 4817–4831, Jun. 2018.
[12] H. Jafarian, S. Bhowmik, and B. Parkhideh, "Hybrid current-/voltage-mode control scheme for distributed ac-stacked PV inverter with low-bandwidth communication requirements," *IEEE Trans. Ind. Electron.*, vol. 65, no. 1, pp. 321–330, Jan. 2018.
[13] Y. Sun *et al.*, "An f-P/Q droop control in cascaded-type microgrid," *IEEE Trans. Power Syst.*, vol. 33, no. 1, pp. 1136–1138, Jan. 2018.
[14] C. D. Townsend, T. J. Summers, and R. E. Betz, "Control and modulation scheme for a cascaded H-bridge multi-level converter in large scale photovoltaic systems," in *Proc. IEEE Energy Convers. Congr. Expo.*, Sep. 2012, pp. 3707–3714.
[15] S. B. Kjaer, J. K. Pedersen, and F. Blaabjerg, "A review of single-phase grid-connected inverters for photovoltaic modules," *IEEE Trans. Ind. Appl.*, vol. 41, no. 5, pp. 1292–1306, Sep./Oct. 2005.
[16] B. Xiao, J. Mei, C. Riley, L. M. Tolbert, and B. Ozpineci, "Modular cascaded H-bridge multilevel PV inverter with distributed MPPT for grid-connected applications," *IEEE Trans. Ind. Appl.*, vol. 51, no. 2, pp. 1722–1731, Mar./Apr. 2015.
[17] L. Zhang, K. Sun, Y. W. Li, X. Lu, and J. Zhao, "A distributed power control of series-connected module-integrated inverters for PV grid-tied applications," *IEEE Trans. Power Electron.*, vol. 33, no. 9, pp. 7698–7707, Sep. 2018.
[18] Y. Yu, G. Konstantinou, C. D. Townsend, and V. G. Agelidis, "Comparison of zero-sequence injection methods in cascaded H-bridge multilevel converters for large-scale photovoltaic integration," *IET Renewable Power Gener.*, vol. 11, no. 5, pp. 603–613, 2017.
[19] U. Borup, F. Blaabjerg, and P. N. Enjeti, "Sharing of nonlinear load in parallel-connected three-phase converters," *IEEE Trans. Ind. Appl.*, vol. 37, no. 6, pp. 1817–1823, Nov./Dec. 2001.
[20] J. He, Y. W. Li, and F. Blaabjerg, "An enhanced islanding microgrid reactive power, imbalance power, and harmonic power sharing scheme," *IEEE Trans. Power Electron.*, vol. 30, no. 6, pp. 3389–3401, Jun. 2015.
[21] J. He, Y. Li, B. Liang, and C. Wang, "Inverse power factor droop control for decentralized power sharing in series-connected-microconverters-based islanding microgrids," *IEEE Trans. Ind. Electron.*, vol. 64, no. 9, pp. 7444–7454, Sep. 2017.
[22] L. Li *et al.*, "Power factor consistency control for decentralized power sharing in islanded AC microgrids with cascaded inverters," in *Proc. 43rd Annu. Conf. IEEE Ind. Electron. Soc.*, Beijing, China, 2017, pp. 1435–1440.
[23] B. P. McGrath, D. G. Holmes, and W. Y. Kong, "A decentralized controller architecture for a cascaded H-bridge multilevel converter," *IEEE Trans. Ind. Electron.*, vol. 61, no. 3, pp. 1169–1178, Mar. 2014.
[24] F. Lu, B. Choi, and D. Maksimovic, "Autonomous control of series connected low voltage photovoltaic microinverters," in *Proc. IEEE 16th Workshop Control Model. Power Electron.*, 2015, pp. 1–6.
[25] J. Wang, C. Jin, and P. Wang, "A uniform control strategy for the interlinking converter in hierarchical controlled hybrid AC/DC microgrids," *IEEE Trans. Ind. Electron.*, vol. 65, no. 8, pp. 6188–6197, Aug. 2018.
[26] H. Xing, J. Ploeg, and H. Nijmeijer, "Padé approximation of delays in cooperative ACC based on string stability requirements," *IEEE Trans. Intell. Veh.*, vol. 1, no. 3, pp. 277–286, Sep. 2016.
[27] J. He and Y. W. Li, "Generalized closed-loop control schemes with embedded virtual impedances for voltage source converters with LC or LCL filters," *IEEE Trans. Power Electron.*, vol. 27, no. 4, pp. 1850–1861, Apr. 2012.
[28] E. Twining and D. G. Holmes, "Grid current regulation of a three-phase voltage source inverter with an LCL input filter," *IEEE Trans. Power Electron.*, vol. 18, no. 3, pp. 888–895, May 2003.
[29] P. C. Loh and D. G. Holmes, "Analysis of multiloop control strategies for LC/CL/LCL-filtered voltage-source and current-source inverters," *IEEE Trans. Ind. Appl.*, vol. 41, no. 2, pp. 644–654, Mar./Apr. 2005.
[30] J. M. Guerrero, L. G. Vicuna, J. Matas, M. Castilla, and J. Miret, "A wireless controller to enhance dynamic performance of parallel inverters in distributed generation systems," *IEEE Trans. Power Electron.*, vol. 19, no. 4, pp. 1205–1213, Sep. 2004.

Jinwei He received the B.Sc. degree from Southeast University, Nanjing, China, the M.Sc. degree from the Institute of Electrical Engineering, Chinese Academy of Sciences, Beijing, China, and the Ph.D. degree from the University of Alberta, Edmonton, AB, Canada, all in electrical engineering, in 2005, 2008, and 2013, respectively.

In September 2015, he joined Tianjin University, Tianjin, China, where he currently is a Professor. His research interests include power electronics for microgrid and distributed power generation.

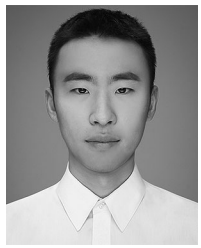

Xiaohui Liu received the B.Sc. degree in automation from Shandong University, Jinan, China, in 2018, and is currently working toward the M.Sc. degree in electrical engineering at Tianjin University, Tianjin, China.

His current research interests include series converter in microgrid and renewable energy power generation.

Chaoxu Mu (M'15–SM'18) received the Ph.D. degree in control science and engineering from Southeast University, Nanjing, China, in 2012.

She was a Visiting Ph.D. Student with the Royal Melbourne Institute of Technology University, Melbourne, VIC, Australia, from October 2010 to November 2011, and was a Postdoctoral Fellow with the Department of Electrical, Computer, and Biomedical Engineering, The University of Rhode Island, Kingston, RI, USA, from December 2014 to August 2016. She is currently an Associate Professor with the School of Electrical and Information Engineering, Tianjin University, Tianjin, China. Her current research interests include nonlinear system control and optimization, adaptive and learning systems, and smart grids.

Chengshan Wang (SM'11) received the Ph.D. degree in electrical engineering from Tianjin University, Tianjin, China, in 1995.

He is currently a Professor with the School of Electrical and Information Engineering, Tianjin University. His research interests include distributed generation and microgrids, power distribution system analysis and planning, and power system security analysis.